NASA TECHNICAL MEMORANDUM

NASA TM 73705

NASA TM 73705

FRICTION, DEFORMATION AND FRACTURE OF SINGLE-CRYSTAL SILICON CARBIDE

by Kazuhisa Miyoshi
Kanazawa University
Kanazawa, Japan

and

Donald H. Buckley
Lewis Research Center
Cleveland, Ohio 44135

TECHNICAL PAPER to be presented at the
Joint Lubrication Conference
cosponsored by the American Society of Lubrication Engineers
and the American Society of Mechanical Engineers
Kansas City, Missouri, October 3-5, 1977

FRICTION, DEFORMATION AND FRACTURE OF SINGLE-CRYSTAL SILICON CARBIDE

by Kazuhisa Miyoshi* and Donald H. Buckley**

ABSTRACT

An investigation was conducted to determine the nature of the deformation and fracture of silicon carbide, and its effects on friction properties. Friction experiments were conducted with hemispherical and conical diamond riders sliding on the basal plane of silicon carbide. The results indicate that, when deformation is primarily elastic, the friction does not depend on crystallographic orientation and there is no detectable fracture or cracking. When, however, plastic deformation occurs, silicon carbide exhibits anisotropic friction and deformation behavior. Surface fracture crack patterns surrounding wear tracks are observed to be of three types. The crack-geometries of two types are generally independent of orientation, the third crack, however, depends on the orientation. All surface cracks extend into subsurface. Anisotropic friction, deformation and fracture on the basal plane are primarily controlled by the slip system $\{10\bar{1}0\}\langle 11\bar{2}0\rangle$ and a cleavage of $\{10\bar{1}0\}$.

---

*National Research Council - National Aeronautics and Space Administration Research Associate; Kanazawa University, Kanazawa, Japan.

**Head, Lubrication Fundamentals Section, NASA Lewis Research Center, Cleveland, Ohio 44135.

STAR Category 27

INTRODUCTION

For many years, it has been known that silicon carbide has outstanding mechanical and physical properties. The uses of silicon carbide include grinding wheels, turbine blades, vanes, and shrouds in gas turbine engines. The considerable recent interest in silicon carbide in the field of tribology has been stimulated mainly by one of its key properties, that is, its high wear resistance under a variety of exacting enviornmental conditions. But, the tribophysical properties of silicon carbide in contact with metals, ceramics and polymers are not clearly understood. Very little experimental work has been done with silicon carbide to determine these properties. Silicon carbide in contact with silicon carbide exhibits lower friction than unlubricated metals and retains it to much higher temperatures (1 and 2). Furthermore, the effect of crystallographic orientation and load on the Knoop microhardness of single-crystal silicon carbide has been invesigated (3). Nevertheless, there is a great lack of fundamental information relative to the mechanism of friction and mechanical behavior of silicon carbide.

Detailed examination, by the present authors of single-crystal silicon carbide in sliding contact with titanium and silicon carbide itself revealed evidence for the formation of silicon carbide wear debris. Further, the wear debris of silicon carbide once formed, plows the silicon carbide surface itself, and grooves are produced in a plastic manner on the surface of the silicon carbide. Thus, it would be of interest to know the friction, deformation and fracture

behavior of silicon carbide, an inherently brittle material, and to compare that behavior with metals, which are ductile. In addition, knowledge of the influence of crystallographic orientation on friction and deformation behavior of silicon carbide may assist in gaining a better abrasion resistance material for use in practical applications (e.g. grinding). Wear of abrasives such as silicon carbide occurs in such operations as grinding, and it is highly desirable to minimize this wear.

This investigation was conducted to examine the friction, deformation and fracture behavior of single-crystal silicon carbide in contact with a diamond rider. Orientation of silicon carbide was also examined relative to its effect on friction and deformation. All experiments were conducted with light loads of 5 to 50 grams, at a sliding velocity of 3 mm/min in dry argon (H_2O less than 20 ppm) at atmospheric pressure on the (0001) basal plane in the $\langle 10\bar{1}0 \rangle$ and $\langle 11\bar{2}0 \rangle$ directions. The diamond riders used were both spherical and conical. The silicon carbide was subjected to single-pass sliding by the diamond rider and the sliding distance was 2 mm. Studies were all conducted at room temperature.

MATERIALS

The single-crystal silicon carbide platelets used in these experiments were a 99.9 percent pure compound of silicon and carbon (Table I). The silicon carbide has a hexagonal close-packed crystal structure. The C direction was perpendicular to the sliding interface with the basal plane therefore parallel to the interface. The Knoop

hardness is 2954 in the $\langle 10\bar{1}0 \rangle$ and 2917 in the $\langle 11\bar{2}0 \rangle$ directions on the basal plane of silicon carbide (4).

The diamonds were commercially purchased. Diamond is the hardest know material (5). It indents silicon carbide without itself suffering permanent deformation. Also, its elastic constants are very high. With silicon carbide, Young's modulus is about 4.5×10^5 N/mm^2 (6), whilst for diamond it lies between 7 and 10×10^5 N/mm^2 (7). At low sliding velocity in argon at atmospheric pressure the adhesion of diamond to silicon carbide is very low.

EXPERIMENTAL APPARATUS AND PROCEDURE

The apparatus used in this investigation was a system capable of applying load and measuring friction in argon at atmospheric pressure. The mechanism for measuring friction is shown schematically in Fig. 1. The beam contains one flat machined normal to the direction of friction application. The end of the rod contains the diamond rider. The load is applied by placing dead weights on a pan on top of the rod. Under an applied load the friction force is sensed by strain gages.

The single-crystal silicon carbide was mechanically polished with 1 μm Al_2O_3 powder. The diamond riders were both spherical and conical. Three different radii of curvature of spherical riders were used. These were 0.02, 0.15 and 0.3 mm. The apical angle of conical riders was about 120 degrees and the radius of curvature at the apex was less than 5 μm. These were polished with 1 μm Al_2O_3 powder before each friction experiment. Both silicon carbide and diamond surfaces were rinsed with water and 200-proof ethyl alcohol

prior to use. The friction experiments were single-pass. Experiments were conducted with a total sliding distance of 2 mm, at a sliding velocity of 3 mm/min.

RESULTS AND DISCUSSION

Friction, Deformation and Fracture Behavior

Friction and Elastic and Plastic Deformation

Sliding friction experiments were conducted with a spherical diamond rider with a radii of 0.3, 0.15, and 0.02 mm in contact with a flat of silicon carbide, on the (0001) plane in the $\langle 11\bar{2}0 \rangle$ and $\langle 10\bar{1}0 \rangle$ directions. The coefficients of friction measured at various loads are presented in Fig. 2. With a rider of radius of 0.3 mm the coefficient of friction is not constant but decreases as the load increases. The friction is generally very low. The coefficient of friction is about 0.08 at a load of 5 grams and decreases to about 0.03 at a load of 50 grams. It might be anticipated from the friction results that the sliding truly occurred at the interface and an elastic deformation could occur in both silicon carbide and diamond accounting for the low friction observed. In fact, over the entire load range, when a rough estimate is made, the mean contact pressure is about 150 to 350 kg/mm^2. The maximum pressure at the center according to Hertz (8) will be about 230 to 490 kg/mm^2. Further, to a first approximation for the load range investigated, the relation between coefficient of friction (μ) and load (W) is given by an expression of the form: $\mu = KW^{c-1}$ ($c - 1 \doteqdot -1/3$). The inverse minus 3 power may be interpreted most simply as arising from an adhesion mechanism, the area

of contact being determined by elastic deformation herein (5). It should further be noted that even at the high magnifications (up to 10,000 times) of the scanning electron microscope no groove formation due to plastic flow and no cracking of silicon carbide with sliding was observed. The results obtained herein with a spherical diamond rider of radius 0.3 mm in sliding contact with silicon carbide show that silicon carbide can primarily deform elastically.

With riders of radii of 0.15 and 0.02 mm the friction is not constant but increases as the load increases. To a first approximation for this load range the relation between coefficient of friction (μ) and load (W) is given by the expression: $\mu = KW^{c-1}$. The index c depends upon the radius of curvature of the rider. The value of c is approximately 1.3 for riders of radii 0.02 and 0.15 mm. The value of c indicates that the friction is due to shearing and plowing of silicon carbide with the diamond rider. Further, it might be anticipated the plastic deformation could occur in silicon carbide (9). The experimental evidence establishes that permanent grooves in silicon carbide are formed during sliding as seen in Fig. 3. Figure 3 presents surface replication electron micrographs of a wear track generated by the diamond spherical rider with a radius 0.02 mm and at loads 30 grams and 40 grams. It becomes obvious from an examination of Fig. 3 that plastic deformation occurs in silicon carbide. The calculated mean contact pressure, at the load of 50 grams with the rider of radius 0.02 mm, is about 2000 kg/mm^2. The maximum pressure at the center would be about 3000 kg/mm^2 (yield pressure of silicon carbide).

When a rider having a radius 0.15 mm was used in these same experiments, small permanent grooves in silicon carbide were formed during sliding at the load of 50 grams. These observations and the friction results with a diamond rider of radius 0.15 mm in sliding contact with silicon carbide show that silicon carbide can deform both elastically and plastically over the contact area.

Thus, with diamond riders of radii of 0.15 and 0.02 mm the sliding truly occurred at the interface and the friction is due to shearing adhesive bonds at the interface and plowing of silicon carbide.

Figure 3 also indicates surface cracking observed at loads of 30 and 40 grams. At 40 grams load, however, two types of cracks are observed. One type is characterized by being very small in size, is observed in the wear track and propagates perpendicular to the sliding direction, indicated by P in Fig. 3(b).

The second type is a crack, primarily observed on both sides of the wear track, propagating outward from the wear track indicated by S in Fig. 3(b). These small cracks zig-zag along cleavage planes of $\{10\bar{1}0\}$ (see the Z in Fig. 3(b)). With a rider of radius of 0.02 mm, and with a load of less than 20 grams no cracks were observed. Similarly a rider of radius of 0.15 mm no visible cracks were also observed over the entire load range. When, however, a rider of radius of 0.02 mm, was used and the load was above 30 grams, visible cracks were observed as indicated in Fig. 3(a). The first sign of cracking was the formation of a crack in the wear track (P). Thus, the critical load for crack formation during sliding was 30 grams.

The subject of crack formation will be explained in more detail in a later section.

Friction and Plastic Deformation and Fracture

Sliding friction experiments were conducted with conical diamond riders in contact with flat of silicon carbide (0001) surface. The friction traces for light loads of 5, 10 and 20 grams are characterized by randomly fluctuating behavior with no evidence or only occasional evidence of stick-slip. However, friction traces for heavier loads of 30, 40 and 50 grams were primarily characterized by a continuous marked stick-slip behavior. The coefficient of friction was generally low when stick-slip was absent (see average fluctuating-friction in Fig. 4). In the absence of stick-slip, the sliding appeared to involve a plastic flow with a small amount of cracking. Further, the deformation and surface cracking were almost the same as that observed with a spherical rider of radius 0.02 mm above the load of 30 grams as already discussed.

By contrast, the coefficient of friction, which has a marked stick-slip behavior at heavy loads, is high (see average maximum-peak-height in Fig. 4). With increasing loads, the coefficient of friction increases to an equilibrium value of 0.6 to 0.9. The value depends on the sliding direction, as indicated in Fig. 4. This friction process is accompanied by both gross surface cracking and plastic deformation as indicated in Fig. 5. Increasing loads results in increased fracture. Figure 5 shows a scanning electron micrograph of weak track and fragments of silicon carbide generated by the diamond conical rider at a load of 50 grams. Considerable fracture of the surface due to

cleavage occurs. In addition thereto, the heavily deformed groove observed in the central region of the wear track is due to plastic flow. Under such conditions, both large (several microns in size) and small fragments (submicron in size) are generated.

The foregoing results reveal that plastic deformation and fracture in silicon carbide are responsible for the friction behavior observed. Further, these studies show that the coefficient of friction is influenced by the bulk properties of silicon carbide (friction dependency on crystallographic orientation). This subject will be explained in detail later.

Crack Geometry and Mechanism of Fracture

Surface Cracking

As indicated in the previous section, the sliding of the conical rider or spherical rider (radius of 0.02 mm) produces both plastic deformation and cracking on fracture in silicon carbide. The basic concept of deformation of silicon carbide is expressed in the scheme of Fig. 6 (10). Below the rider the material behaves as an outwardly expanding "core" exerting an uniform hydrostatic pressure on its surroundings. The core is an ideally plastic region within which full plastic yielding occurs. The contact pressure and the mean pressure in the core are the same as the yield pressure (about 2500 to 3000 kg/mm^2), that is, about 3Y where Y is the yield stress of silicon carbide (8).

Beyond the plastic yielding zone lies the elastic "matrix". At the elastic-plastic boundary, elastic and plastic strains are of comparable magnitude. The mean pressure is nearly 1.1 at this stage. The mean

pressure increases from a value of about 1.1 Y to about 3Y as the deformation passes from the onset of plastic deformation to a fully plastic state.

The surface crack patterns surrounding the wear tracks (plastic grooves) made by spherical rider and conical rider were three types as schematically indicated by P, S and L in Fig. 7. In addition to the two types of surface cracks shown in the former section (P and S), a crack (L) propagating parallel to the sliding direction is also observed (Fig. 8). The geometrics of the cracks P and L are generally independent of the crystallographic orientation. The crack P propagates perpendicular to the sliding direction in the wear track. The crack L propagates parallel to it, that is, along the sliding direction in the central portion of the wear track. As the crack L are generally covered with a plastic deformed layer, they cannot be observed without etching of the wear track or cross-sectioning of the wear track.

From reference 11 the initiation of each crack and the crack geometry may be determined by the maxima in tensile stresses in the contact zone or surrounding wear track. It seems reasonable to suppose that cracks will tend to initiate at one of these favored locations.

The surface cracks S, start from maxima tensile stress fields (11), however, the propagation of these cracks depends on the crystallographic orientation. The cracks generally propagate along cleavage planes of $\{10\bar{1}0\}$ as shown in Figs. 3(b) and 8. Figure 8 presents a scanning electron micrograph of a weak track generated by the diamond conical rider. The specimen surface was lightly etched

with molten salt ($1NaF + 2KCO_3$) at 700^{o} to 800^{o} C. In Fig. 8, surface crack P in the wear track, S at the both sides of the wear track, and L in the central portion of the wear track are observed. Most of the cracks of the S type are observed on both sides of the wear track and propagate outward from the wear track along $\{10\bar{1}0\}$ planes.

Subsurface Cracking

All surface cracks propagate subsurface as schematically indicated in Fig. 7(b) and (c). Figure 7(b) and (c) summarize lateral and longitudinal cross-sectional views of the wear track.

In the lateral cross-section (Fig. 7(b)), the cracks S and L appear to progagate subsurface and straight downward (at the normal right angle to the specimen surface). These cracks continue to extend out of the primary plane. In some instances, however, crack diversion will occur along a weak plane in silicon carbide, for example, the basal plane. Thus, crack growth subsurface may occur by secondary fracture mechanisms.

Figure 9 is a lateral cross-section view through a wear track in silicon carbide. It serves to confirm the geometries of cracks. The crack S has grown straight downward (primary crack) and the tip of crack subsurface becomes curved and progagates along the secondary weak plane, (secondary crack, B), that is, the basal plane. The crack then propagates parallel to the sliding surface of the specimen.

Figure 10 is a lateral cross-section view. It indicates that the crack L has grown straight downward along the contact axis of the

rider underneath the wear track as shown in Figs. 10(a) to (d). An increase in load causes, further, stable growth of the crack L. In a comparison of Figs. 10(b) and (d), the crack propagation - length in the subsurface region at the load of 10 grams is a factor of 1/3 of that at the load of 30 grams. The crack L, as for the crack S, has grown straight downward (primary crack) and the tip of crack become curved and propagates along the secondary weak plane (secondary crack). That is, the crack grows along the basal plane and parallel to the sliding surface of the specimen as shown in Figs. 10(c) and (d).

Thus, the initiation and propagation of the crack L may occur in accordance with 3 terms: (1) the sharp point of the rider produces an plastic deformation region; (2) at some initiation point, a deformation-induced flaw develops into a small crack on the contact axis of the rider underneath the wear track and (3) an increase in load causes stable growth of the crack.

Figure 11 reveals the fracture in a lateral cross-section. The fracturing of silicon carbide is the result of primary cracks (S and L) and secondary cracks (B) being generated, propagating and then intersecting.

In the longitudinal cross-section view as was schematically shown in Fig. 7(c), the crack P appears to propagate subsurface. The cracks P (primary cracks) become curved during crack propagation as the cracks L and S. The tips of the cracks propagate along the secondary weak plane (secondary crack, B), that is, the basal plane parallel to the sliding surface of the specimen. Figures 12(a) to (c) are the longi-

tudinal cross-sectional view through a wear track of silicon carbide. It serves to confirm the geometries of crack P. The crack S has grown straight downward and the tips of the crack become curved and propagate along the basal plane as shown in Fig. 12(a) and as was previously observed. Figure 12(b) also shows the result of primary cracks (P) and secondary cracks (B) being generated, propagating, and then intersecting. Figure 12(c) reveals that the cracks are generated in and confined to elastic matrix of the subsurface region of silicon carbide specimen and as indicated by B (about 30 μm in depth). It is of interest to note that such a subsurface crack is produced at the depth of 30 μm from the specimen surface in the bulk.

Mechanism of Fracture

The fracturing of the silicon carbide surface is the result of cracks being generated, propagating and then intersecting. Figure 13(a) shows a scanning electron micrograph of the wear track and wear debris before gross sliding. In this case, both the loading and tangential force were applied to the specimen, but no gross sliding was observed.

In Fig. 13(a), a sector-shaped light area adjacent to and ahead of wear track (plastic indentation) made by rider is a large particle of wear debris which was generated during micro-sliding of rider. A large number of small wear debris particles are also generated during loading and micro-sliding by rider. It is anticipated from Fig. 13(a) that gross fracturing is primarily due to cleavage-cracking along $\{10\bar{1}0\}$ planes (the crack, S) and subsurface-cleavage-cracking (the crack, B) made by micro-sliding of the rider. Further, Figure 13(b)

shows a scanning electron micrograph of wear track and wear debris after gross sliding.

Figure 13(b) reveals the wear debris has been divided (fractured) by gross-sliding of rider, and the wear track is plastically deformed. The gross wear debris has sharp edges generated by cleavage cracking of $\{10\bar{1}0\}$ planes. Figure 13(c) shows the third stage of the fracturing process. One of the gross wear debris particles divided, fractured is ejected from the wear track. The track, where the wear debris particle was ejected reveals that the fracturing is the result of surface cracking (S) as a result of cleavage of $\{10\bar{1}0\}$ planes and subsurface cracking as a result of cleavage along $\{10\bar{1}0\}$ planes. Dislodged gross wear particles could be observed near the wear track as shown in Fig. 13(c).

Figure 14 also reveals the wear tracks accompanied by fracture. Again this is primarily due to surface cracking of $\{10\bar{1}0\}$ planes observed on both sides of the wear track and subsurface cracking of (0001) planes.

Thus, the fracture behavior of silicon carbide during sliding, as mentioned above, may be explained in terms of the fracture energy acting in $\{10\bar{1}0\}$ cleavage system (primary cracking system) during slidings in the $\langle 10\bar{1}0\rangle$ and $\langle 11\bar{2}0\rangle$ directions on a (0001) silicon carbide surface.

Anisotropies of Friction on the Basal Plane

The foregoing results reveal that plastic flow, cleavage and fracture in silicon carbide are the main factors responsible for the

friction behavior observed. Further, these studies show that the coefficient of friction is influenced by the bulk properties of silicon carbide (friction dependency on orientation).

The coefficient of friction was measured as a function of crystallographic direction of sliding on the basal plane (0001) of silicon carbide for various diamond riders and the results obtained are presented in Fig. 15. Anisotropy is governed by two factors: (1) geometry of the rider and (2) load. When the radius of curvature of the spherical rider becomes larger or a lighter load is applied to the sliding surface, (that is, elastic deformation or small amount of plastic flow occurs), the observed friction is low. Further, the anisotropy diminishes as indicated by the results of a spherical diamond rider of radius 0.3 mm at loads of 5 and 30 grams, and radius 0.02 mm at a load of 5 grams in Fig. 15. This type of behavior was also observed with diamond in sliding contact with itself (5).

When higher loads are applied to the spherical rider of smaller radius 0.02 mm or a conical rider is used, penetration of the bulk due to the gross plastic flow occurs and silicon carbide exhibits anisotropic friction and deformation behavior. Observations of silicon carbide surface by optical, scanning electron and replication electron microscopy indicated that the $\langle 11\bar{2}0 \rangle$ direction has the larger weak track due to plastic flow and is the direction of high friction. It is the soft direction on silicon carbide (0001) single-crystal surface.

Microhardness studies by Shaffer (4) and Adewoye et al. (3) also show a similar small anisotropy with greater Knoop hardness in the $\langle 10\bar{1}0 \rangle$ direction than in the $\langle 11\bar{2}0 \rangle$ direction.

The Knoop hardness of the basal plane of silicon carbide is greater than that for any other crystallographic plane in the material (4). It is, therefore, anticipated that the $\langle 10\bar{1}0 \rangle$ directions in the basal plane of silicon carbide will exhibit the greatest abrasion resistance in practical applications, because bulk deformation plays a role in the frictional anisotropy of silicon carbide.

Silicon carbide surfaces for a conical diamond sliding in the $\langle 10\bar{1}0 \rangle$ direction have been etched with molten salt ($1NaF + KCO_3$) at 700° to 800° C to reveal dislocations. One of these surfaces is seen in Fig. 16. Observation of the surface confirms that plastic flow has taken place beyond the actual wear track. In several cases, the existance of straight rows of dislocation etch pits along the $\langle 11\bar{2}0 \rangle$ directions in the (0001) plane is presented in Fig. 16. This is confirmatory evidence that the $\{ 10\bar{1}0 \} \langle 11\bar{2}0 \rangle$ slip system is operating during sliding. Furthermore, the fracturing of silicon carbide during sliding can be also explained in terms of $\{ 10\bar{1}0 \}$ cleavage system during sliding in the $\langle 10\bar{1}0 \rangle$ and $\langle 11\bar{2}0 \rangle$ directions on a (0001) silicon carbide surface as mentioned in an earlier section. Thus, the $\{ 10\bar{1}0 \} \langle 11\bar{2}0 \rangle$ slip system and $\{ 10\bar{1}0 \}$ cleavage system are responsible for the frictional anisotropy observed on the basal plane of silicon carbide.

Several slip systems have been observed in ∂-silicon carbide such as (0001) $\langle 11\bar{2}0 \rangle$, $\{ 33\bar{0}1 \} \langle 11\bar{2}0 \rangle$ (12) and $\{ 10\bar{1}0 \} \langle 11\bar{2}0 \rangle$ (13). The deformation behavior of silicon carbide during sliding, as mentioned above, may be readily explained in terms of the resolved shear stress (14) acting on $\{ 10\bar{1}0 \} \langle 11\bar{2}0 \rangle$ slip systems during slidings of $\langle 10\bar{1}0 \rangle$

and $\langle 11\bar{2}0 \rangle$ directions on a (0001) silicon carbide surface. In addition Adewoye et al. (3) explained the Knoop hardness anisotropy data for the (0001) plane of a ∂-SiC using the resolved shear stress analysis (14). Similar data for Knoop hardness anisotropy of tungsten carbide has been explained by a resolved shear stress calculation involving the $\{10\bar{1}0\}\langle 0001 \rangle$ and $\{10\bar{1}0\}\langle 11\bar{2}0 \rangle$ slip systems (14).

CONCLUSIONS

As a result of the sliding friction experiments conducted in this investigation with single-crystal silicon carbide in sliding contact with spherical and conical diamond riders the following conclusions are drawn:

1. When the radius of curvature of the spherical diamond rider is larger (a rider of radius 0.3 mm), deformation of silicon carbide is principally elastic. Under these conditions the coefficient of friction is low and does not show a dependence on orientation of the silicon carbide. Further, there is no detectable cracking of the silicon carbide surfaces.

2. Where as smaller radius of curvature of spherical diamond rider (riders of radii 0.15 and 0.02 mm) or a conical diamond rider is used plastic grooving occurs and silicon carbide exhibits anisotropic friction and deformation behavior and the coefficient of friction depends on load.

3. The surface crack patterns surrounding wear tracks (plastic grooves) are three types. One type is characterized by a crack propagating perpendicular to the sliding direction (P). The second is a

crack propagating parallel to the sliding direction (L). The geometries of the cracks P and L are generally independent of the crystallographic orientation and depends on the maxima tensile stress fields. The propagation of crack S, however, depends on the crystallographic orientation.

4. All surface cracks continue extension out of the primary plane in subsurface. In some cracks, however, diversion of crack occurs along weak-cleavage-plane in silicon carbide. Thus secondary fracture grows in the subsurface. Further, cracks generated in and confined to subsurface region are observed.

5. Gross fracturing is primarily due to cleavage-cracking of $\{10\bar{1}0\}$ planes (the crack, S) and subsurface-cleavage-cracking (the crack, B).

6. Anisotropic friction, deformation and fracture on the basal plane of silicon carbide are primarily controlled by the slip system $\{10\bar{1}0\}\langle 11\bar{2}0\rangle$ and a cleavage of $\{10\bar{1}0\}$.

7. It is predicted from the foregoing conclusions that the $\langle 10\bar{1}0\rangle$ directions in the basal plane exhibit the greatest resistance to abrasion for the silicon carbide when used in practical applications.

REFERENCES

1. Brookes, C. A. and Imai, M., "The Frictional Properties of Silicon Nitride and Silicon Carbide," in Special Ceramics 1964, P. Popper, ed., Academic Press, 1965, pp. 259-266.

2. Brookes, C. A. and Atkins, A. G., "The Friction and Hardness of Refractory Compounds," in Fifth Plansee Siminar De Re Metallica on Metals for the Space Age, F. Benesovsky, ed., Metallwerk Plansee AG, 1965, pp. 712-720.

3 Adewoye, O. O., et al., "Structural Studies of Surface Deformation in MgO, SiC and Si3N4," Cambridge University, England (AD-A008993), Oct. 1974.

4. Shaffer, P. T. B., "Effect of Crystal Orientation on Hardness of Silicon Carbide," Journal of the American Ceramic Society, 47, 1964, p. 466.

5. Bowden, F. P. and Tabor, D., "The Friction and Lubrication of Solids - Part II," Clarendon Press, Oxford, 1964, pp. 158-185.

6. Hasselman, D. P. H. and Batha, H. D., "Strength of Single Crystal Silicon Carbide," Applied Physics Letters, 2, 1963, pp. 111-113.

7. Bhagavantam, S. and Bhimasenacher, J., "Elastic Constants of Diamond," Proceeding of the Royal Society, A 187, 1946, pp. 381-384.

8. Bowden, F. P. and Tabor, D., "The Friction and Lubrication of Solids - Part I," Clarendon Press, Oxford, 1950, pp. 10-22.

9. Tanaka, K., et al., "Friction and Deformation of Mn - Zn Ferrite Single Crystals," in Proceeding of the JSLE - ASLE International Lubrication Conference, T. Sakurai, ed., Elseview Scientific, Amsterdam, 1975, pp. 58-66.

10. Marsh, D. M., "Plastic Flow in Glass," Proceeding of the Royal Society (London), A 279, 1964, pp. 420-435.

11. Lawn, B. R., "Partial Cone Crack Formation in a Brittle Material Loaded with a Sliding Spherical Indenter," Proceeding of the Royal Society (London), A 299, 1967, pp. 307-316.

12. Anelinckx, S., Strumase, G., and Webb, W. W., "Dislocation in Silicon Carbide," Journal of Applied Physic, 31, 1960, pp. 1359-1370.

13. Brookes, C. A., O'Neill, J. C., and Redfern, B. A. W., "Anisotropy in the Hardness of Single Crystals," Proceeding of the Royal Society (London), A322, 1971, pp. 73-88.

14. French, D. N. and Thomas, D. A., "Hardness Anisotropy and Slip in WC Crystals," Transactions of the Metallurgical Society, AIME, 233, 1965, pp. 950-952.

TABLE I. - COMPOSITION DATA OF

SINGLE-CRYSTAL SILICON CARBIDE

AS GROWN PLATELETS*

Si	C	O	B	P
66.6%	33.3%	<500 ppm	<100 ppm	<200 ppm

Others <0.1 ppm

*Manufacturer's analysis

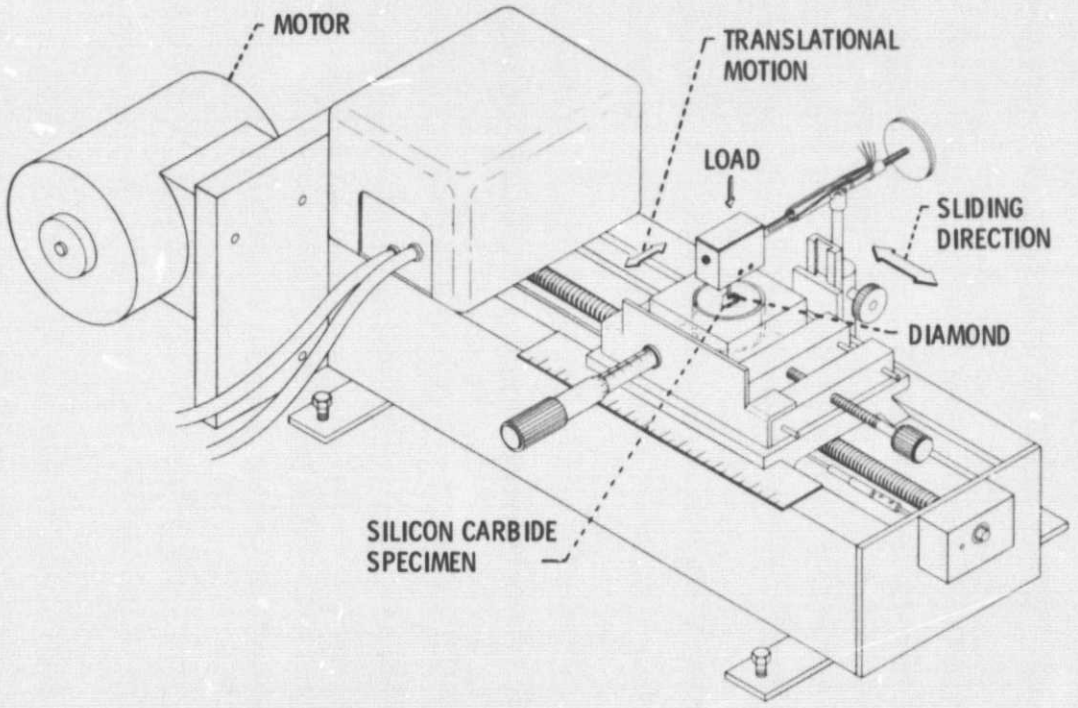

CD-12079-26

Figure 1. - Friction and wear apparatus in argon at atmospheric pressure.

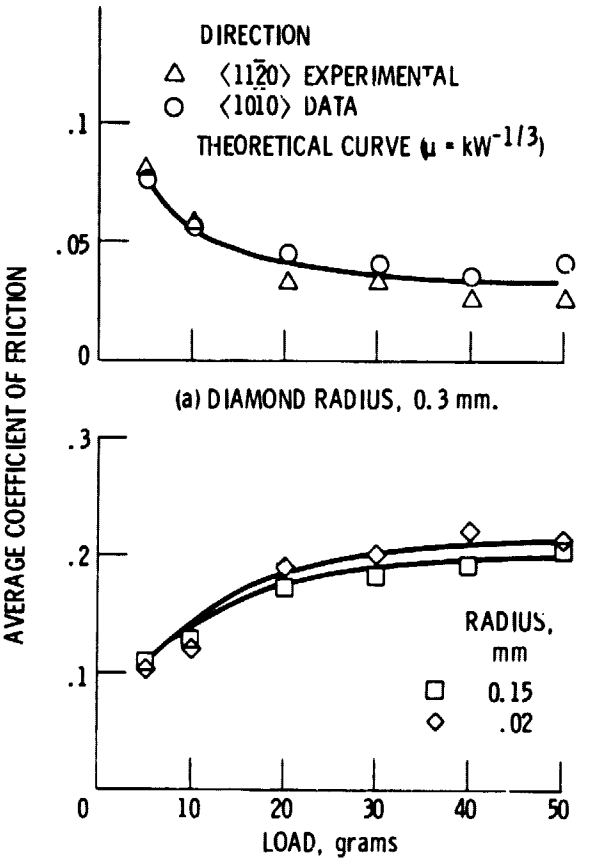

(b) DIAMOND RADII, 0.15 AND 0.02 mm.

Figure 2. - Average coefficient of friction as function of load for spherical diamond riders of different radii sliding on single-crystal silicon carbide (0001) surface. Sliding velocity, 3 mm/min; temperature, 25° C in argon at atmospheric pressure.

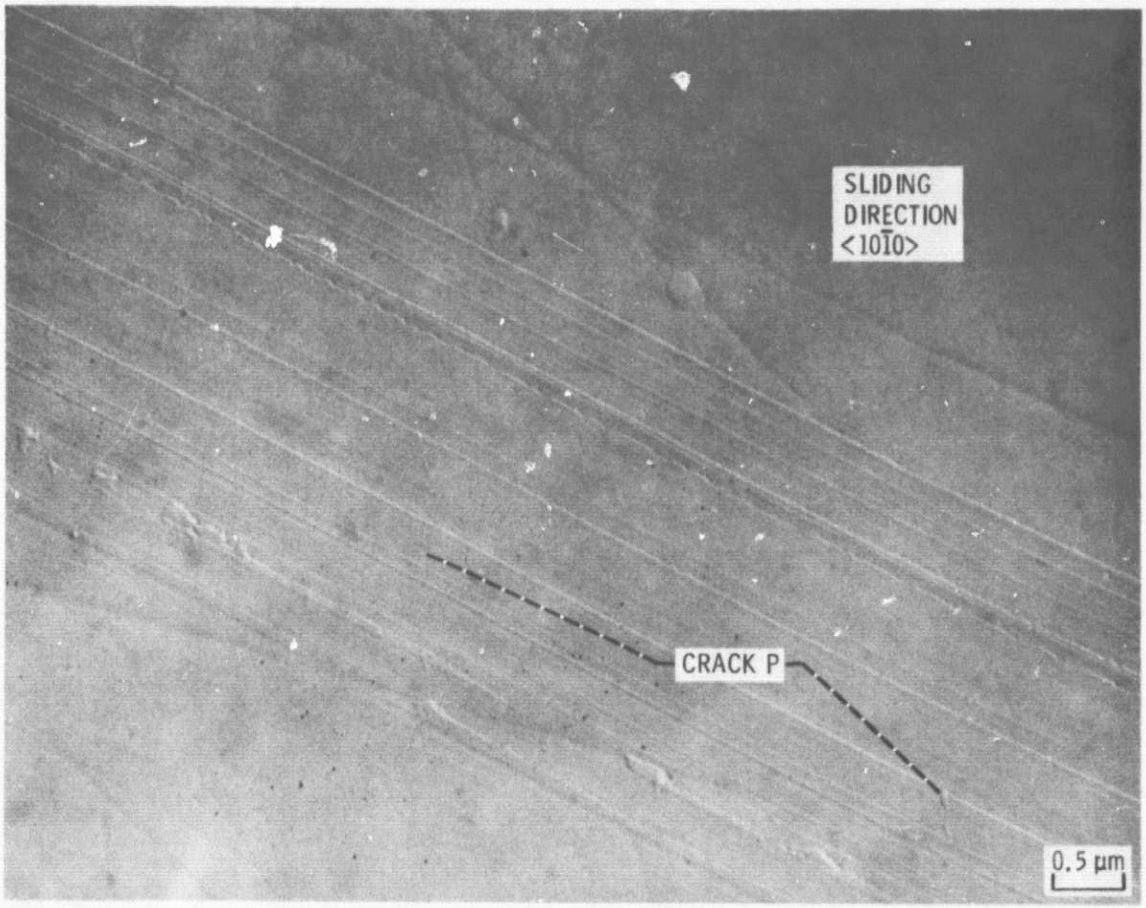

(a) LOAD, 30 GRAMS.

Figure 3. - Replication electron micrographs of wear track on single-crystal silicon carbide (0001) surface. Single pass of spherical rider of radius 0.02 mm; sliding direction, <10$\bar{1}$0>; sliding velocity, 3 mm/min; temperature, 25^0 C in argon at atmospheric pressure.

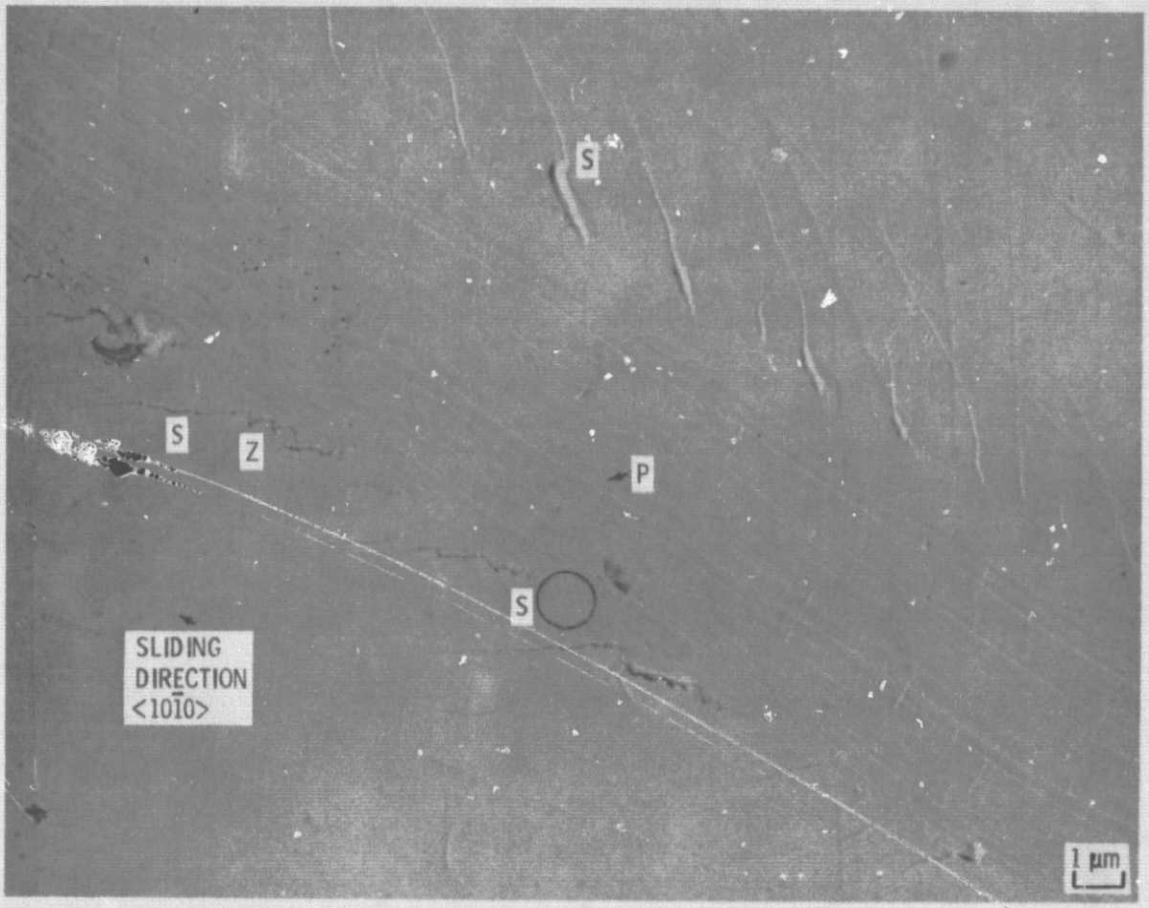

(b) Load, 40 grams.

Figure 3. - Concluded.

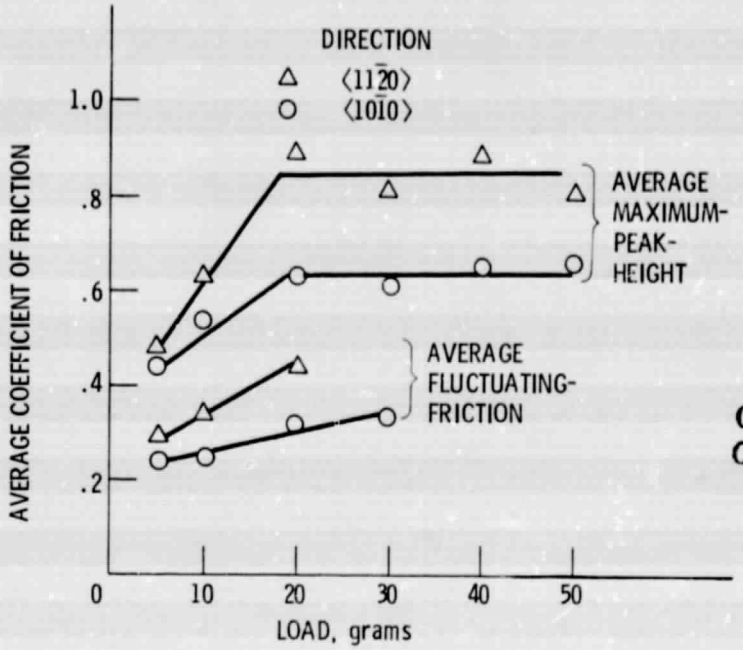

Figure 4. - Average coefficient of friction as function of load for a conical diamond rider sliding on single-crystal silicon carbide (0001) surface in argon at atmospheric pressure. Sliding velocity, 3 mm/min; temperature, 25° C in argon at atmospheric pressure.

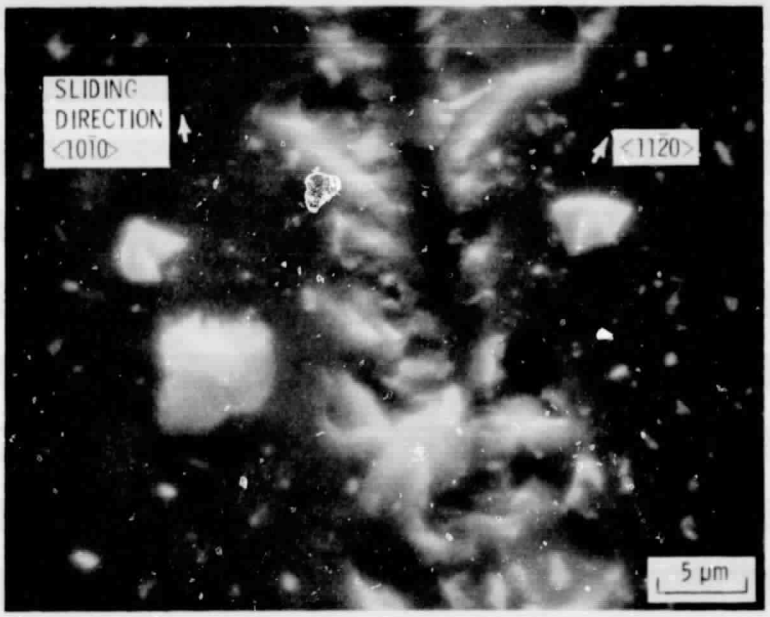

Figure 5. - A scanning electron micrograph of wear track and wear debris on a single-crystal silicon carbide surface. Single pass of conical diamond rider; sliding direction, ⟨10$\bar{1}$0⟩; sliding velocity, 3 mm/min; 50 grams; temperature, 25° C in argon at atmospheric pressure.

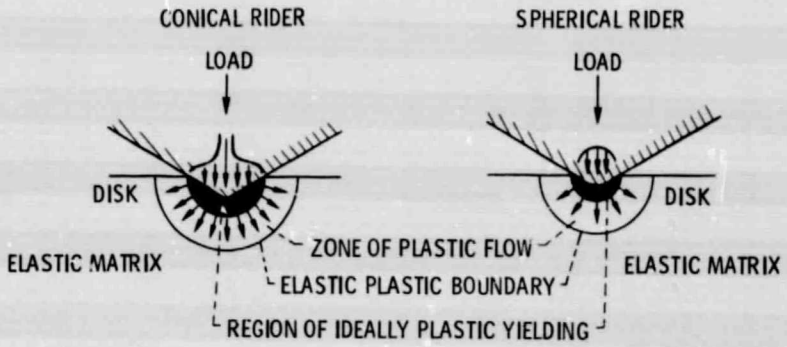

Figure 6. - Models for elastic-plastic groove produced by riders.

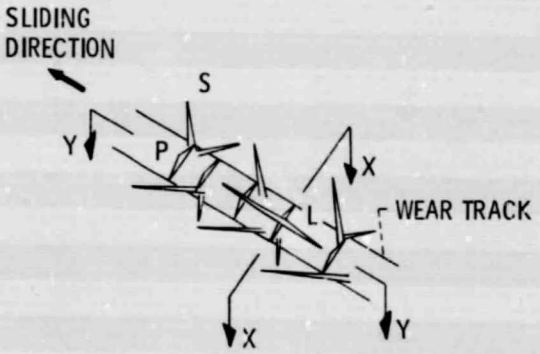

(a) SCHEMATIC REPRESENTATION OF SURFACE CRACKS AND WEAR TRACK, AND ARRANGEMENT OF CROSS-SECTION.

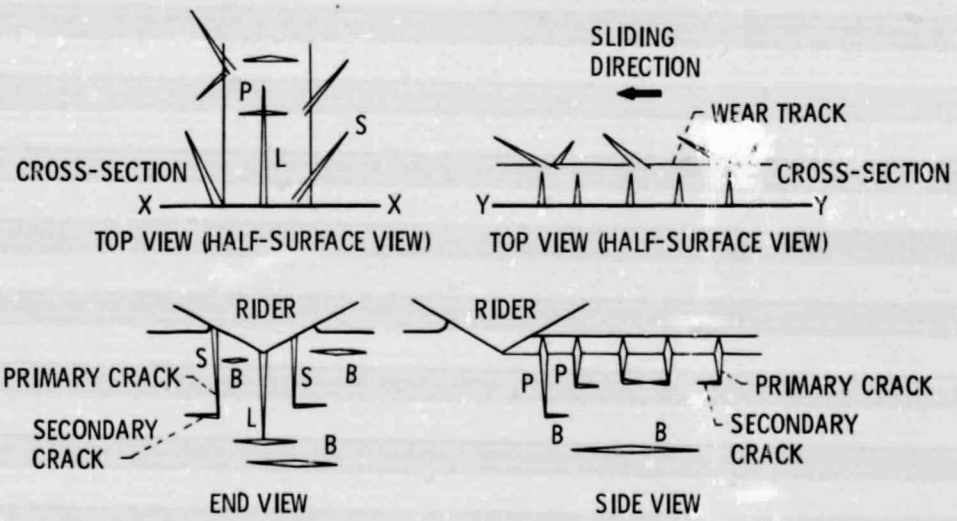

(b) LATERIAL CROSS-SECTION (X-X). (c) LONGITUDINAL CROSS-SECTION (Y-Y).

Figure 7. - Schematic model of surface and subsurface cracking during sliding. P: cracks propagating perpendicular to the sliding direction. S: cracks propagating outward from the wear track. L: cracks propagating parallel to the sliding direction in the wear track. B: cracks generated and propagating in subsurface.

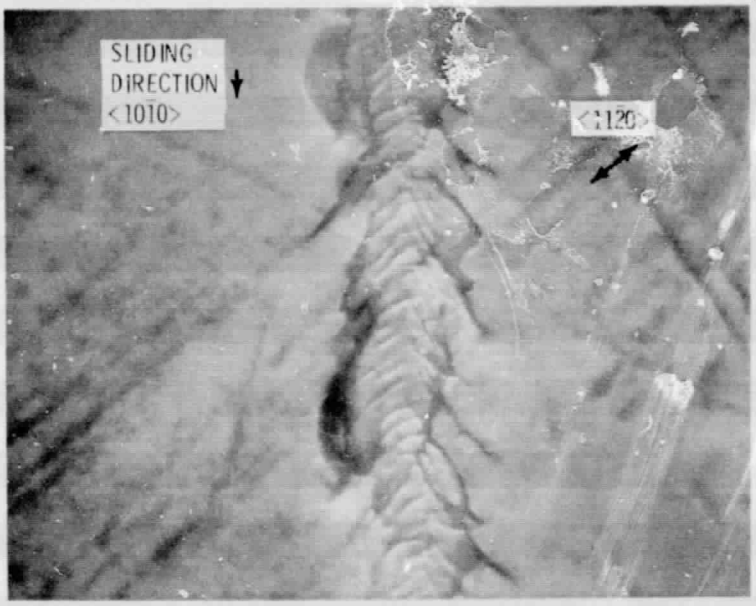

(a) LOAD, 30 GRAMS.

(b) LOAD, 50 GRAMS.

Figure 8. - Scanning electron micrographs of wear track on single-crystal silicon carbide (0001) surface (etched with molten salt (1 NaF + 2 KCO_3) at 700 to 800° C)). Single pass of conical diamond rider; sliding direction, <1010>; sliding velocity, 3 mm/min; temperature, 25° C in argon at atmospheric pressure.

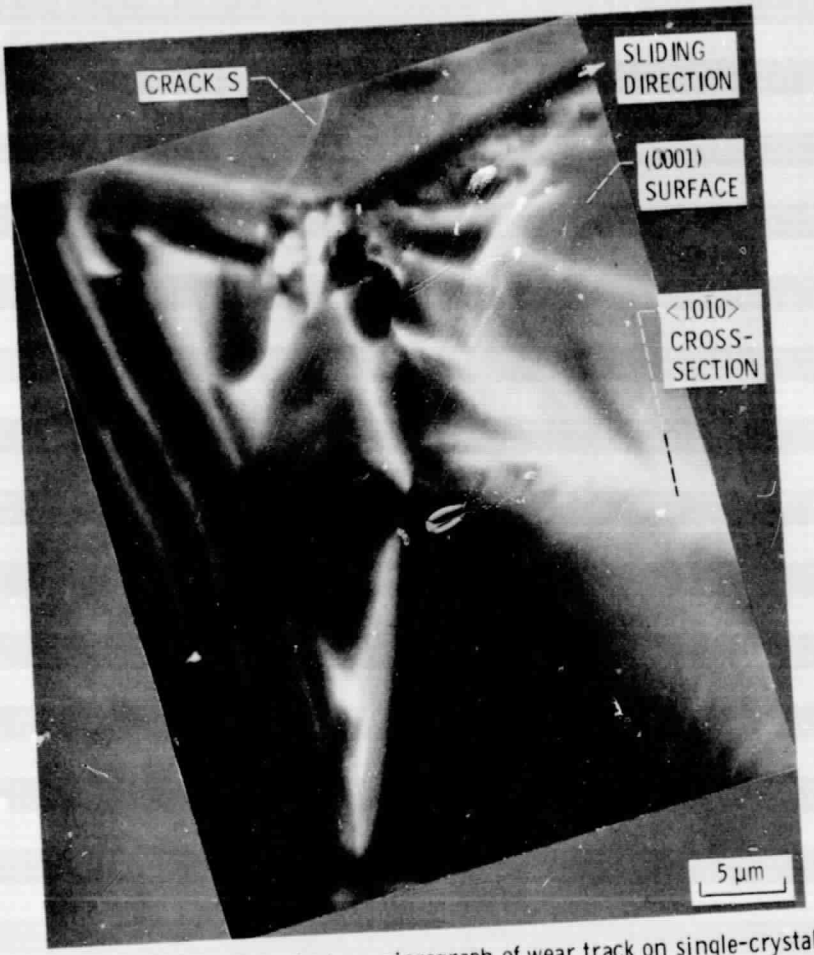

Figure 9. - Scanning electron micrograph of wear track on single-crystal silicon carbide (0001) surface. Lateral cross-section view. Single pass of conical diamond rider; sliding direction, <1010>; sliding velocity, 3 mm/min; load, 30 grams; temperature, 25° C in argon at atmospheric pressure.

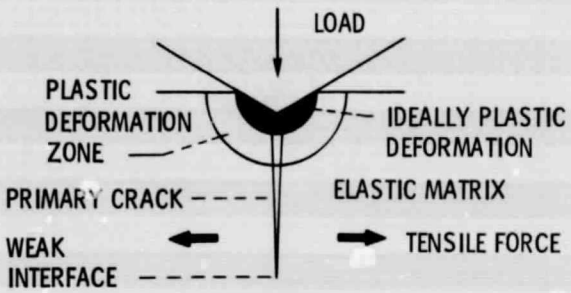

(a) LIGHT LOAD.

(b) LOAD, 10 GRAMS.

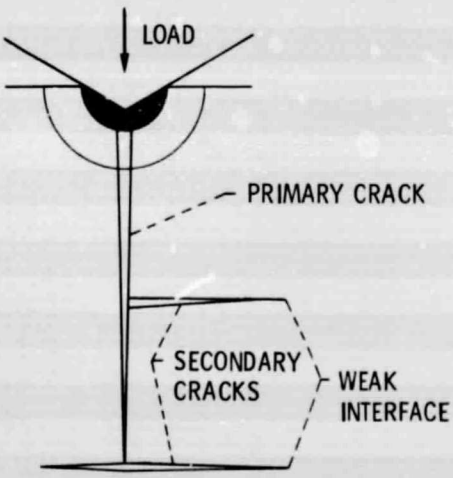

(c) HEAVY LOAD.

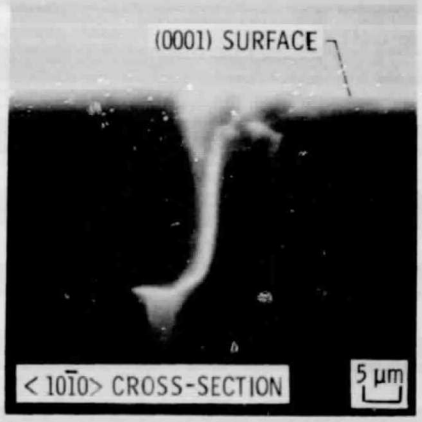

(d) LOAD, 30 GRAMS.

Figure 10. - Lateral cross-section. Single pass of conical diamond rider; sliding direction, <10$\bar{1}$0>; sliding velocity, 3 mm/min; temperature, 25° C in argon at atmospheric pressure.

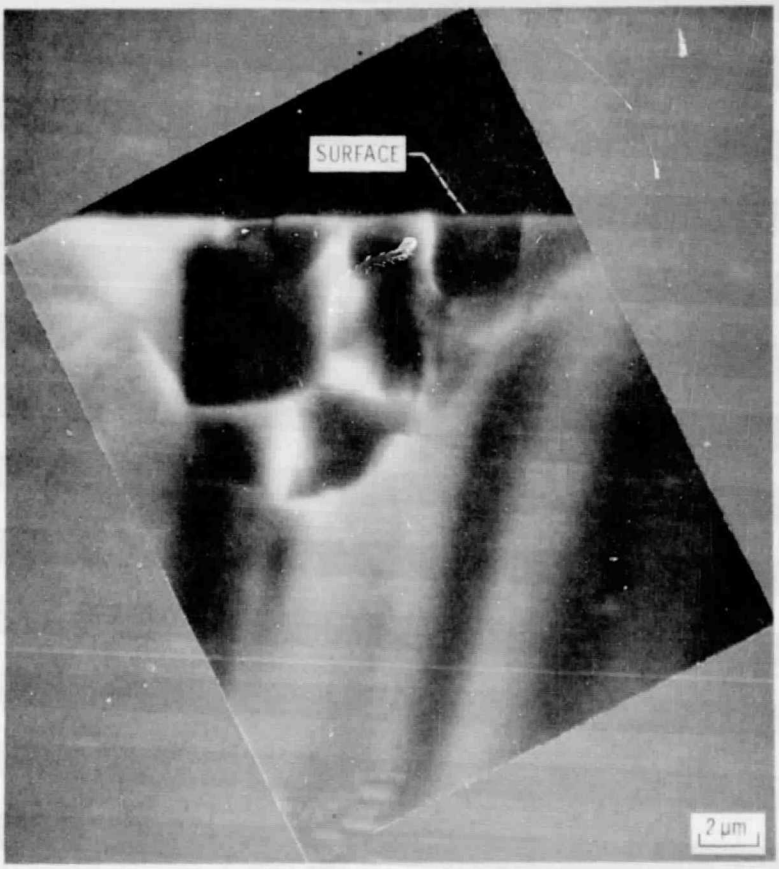

Figure 11. - A scanning electron micrograph of wear track. Lateral cross-section view. Signle pass of conical diamond rider; sliding direction, <1010>; sliding velocity, 3 mm/min; load, 10 grams; temperature, 25^{0} C in argon at atmospheric pressure.

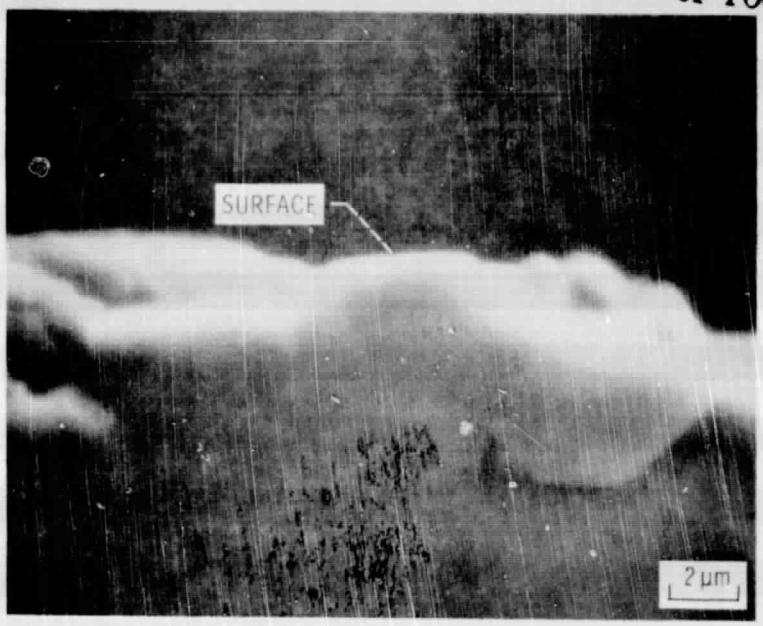

(a) SURFACE CRACK P AND SECONDARY CRACK B.

(b) CRACKS INTERSECTED IN SUBSURFACE.

Figure 12. - Scanning electron micrograph of wear track. Longitudinal cross-section view. Single pass of conical diamond rider; sliding direction, <1010>, sliding velocity, 3 mm/min; load, 30 grams; temperature, 25° C in argon at atmospheric pressure.

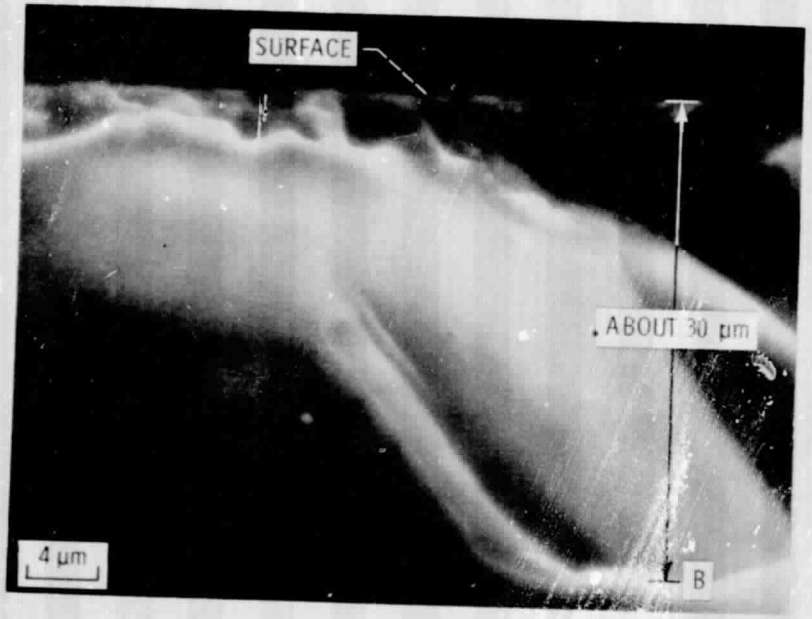

(c) SUBSURFACE CRACK B.

Figure 12. - Concluded.

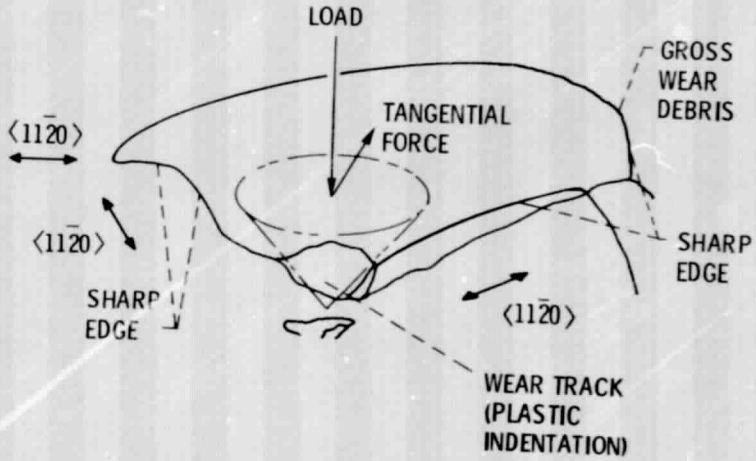

(a) FIRST STAGE (BEFORE GROSS SLIDING).

Figure 13. - Mechanism of fracture. Single pass of conical diamond rider; sliding surface, (0001); sliding direction, $\langle 10\bar{1}0 \rangle$; sliding velocity, 3 mm/min; load, 30 grams; temperature, 25° C in argon at atmospheric pressure.

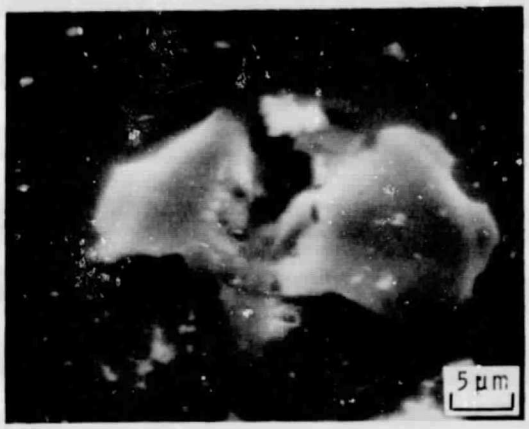

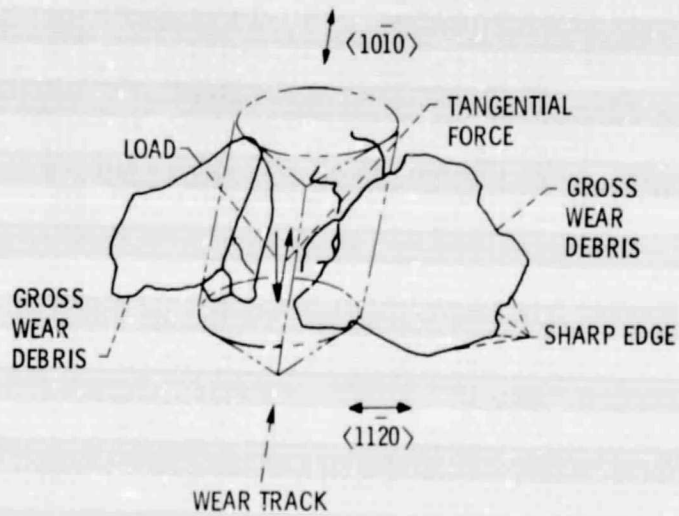

(b) SECOND STAGE (AFTER GROSS SLIDING).

Figure 13. - Continued.

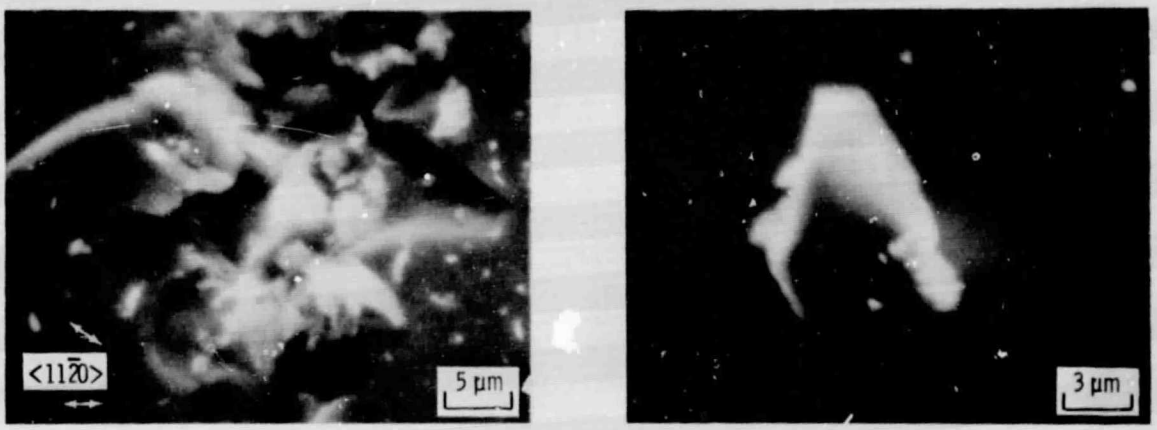

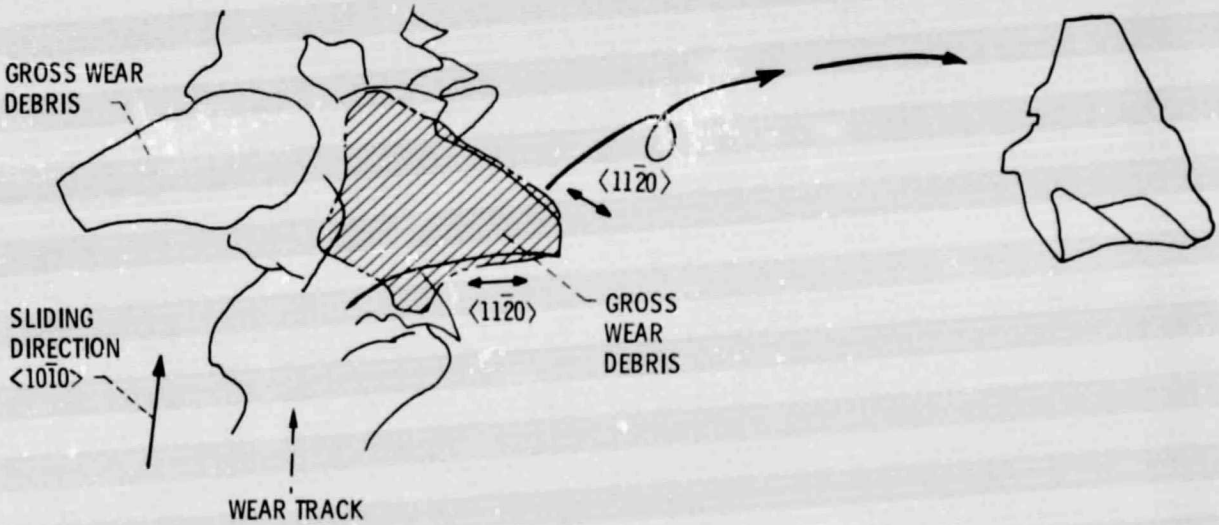

(c) THIRD STAGE.

Figure 13. - Concluded.

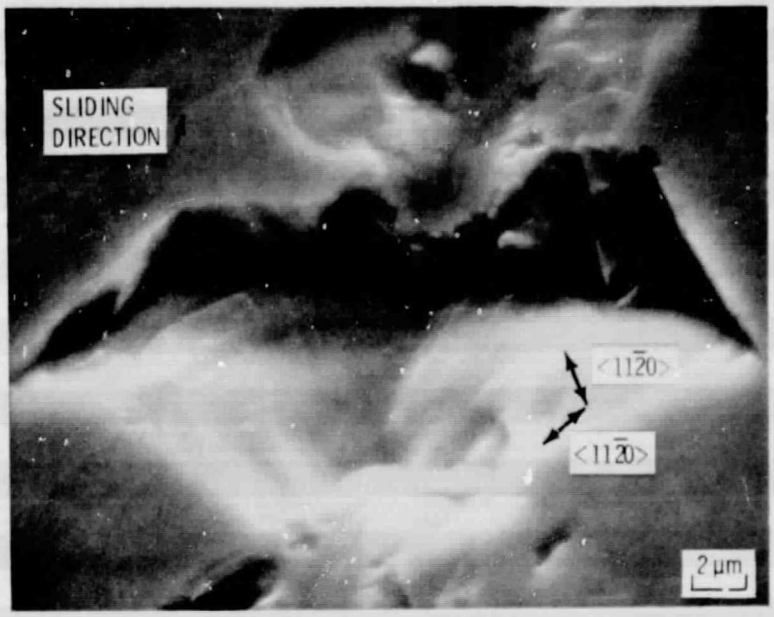

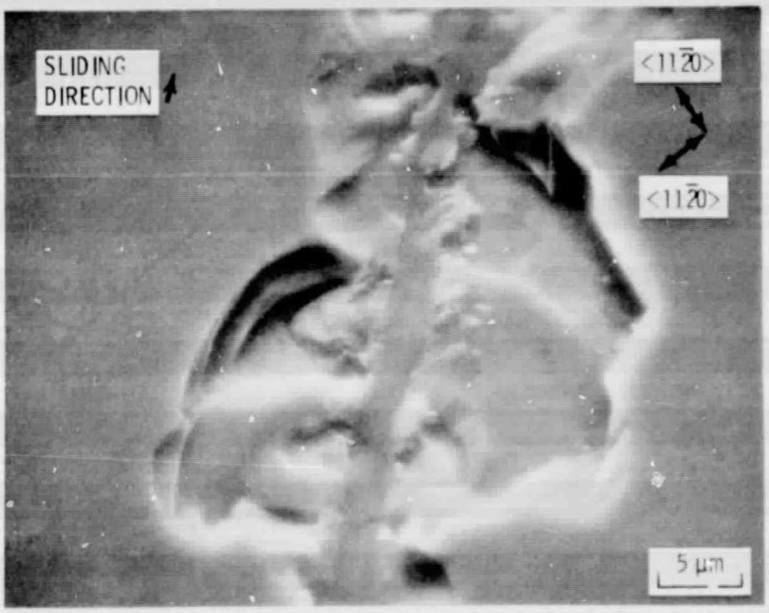

E-9121

Figure 14. - Scanning electron micrographs of wear tracks accompanied with cleavage on a polished (0001) silicon carbide surface. Single pass on conical diamond rider; sliding direction, <10$\bar{1}$0>; sliding velocity, 3 mm/min; load, 50 grams; temperature, 25° C in argon at atmospheric pressure.

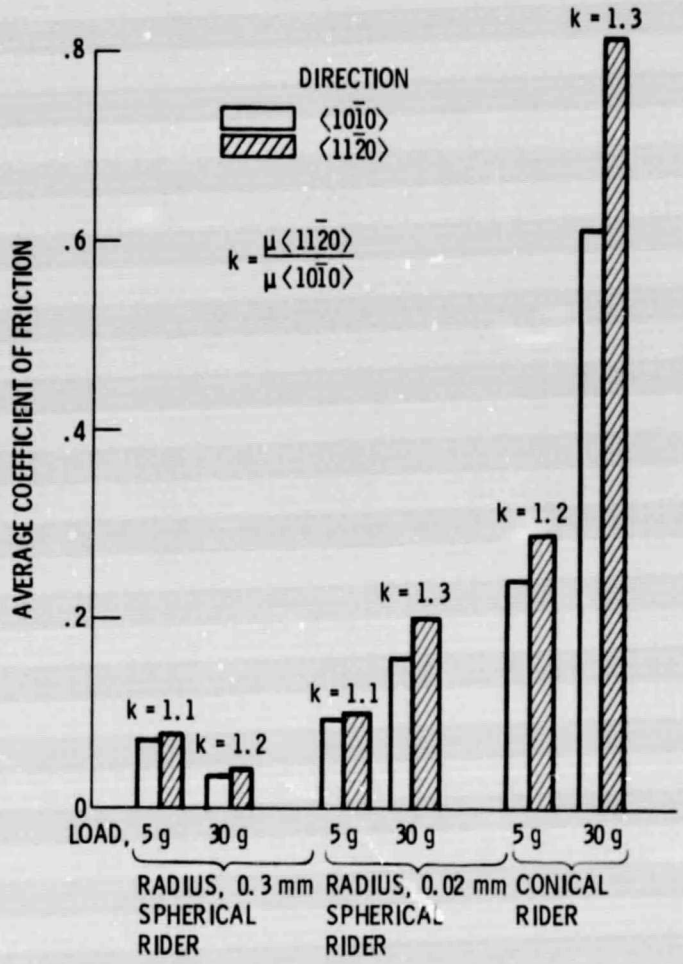

Figure 15. - Friction anisotropy for spherical and conical diamond riders sliding on single-crystal silicon carbide (0001) surface in argon at atmospheric pressure. Sliding velocity, 3 mm/min; temperature, 25° C in argon at atmospheric pressure.

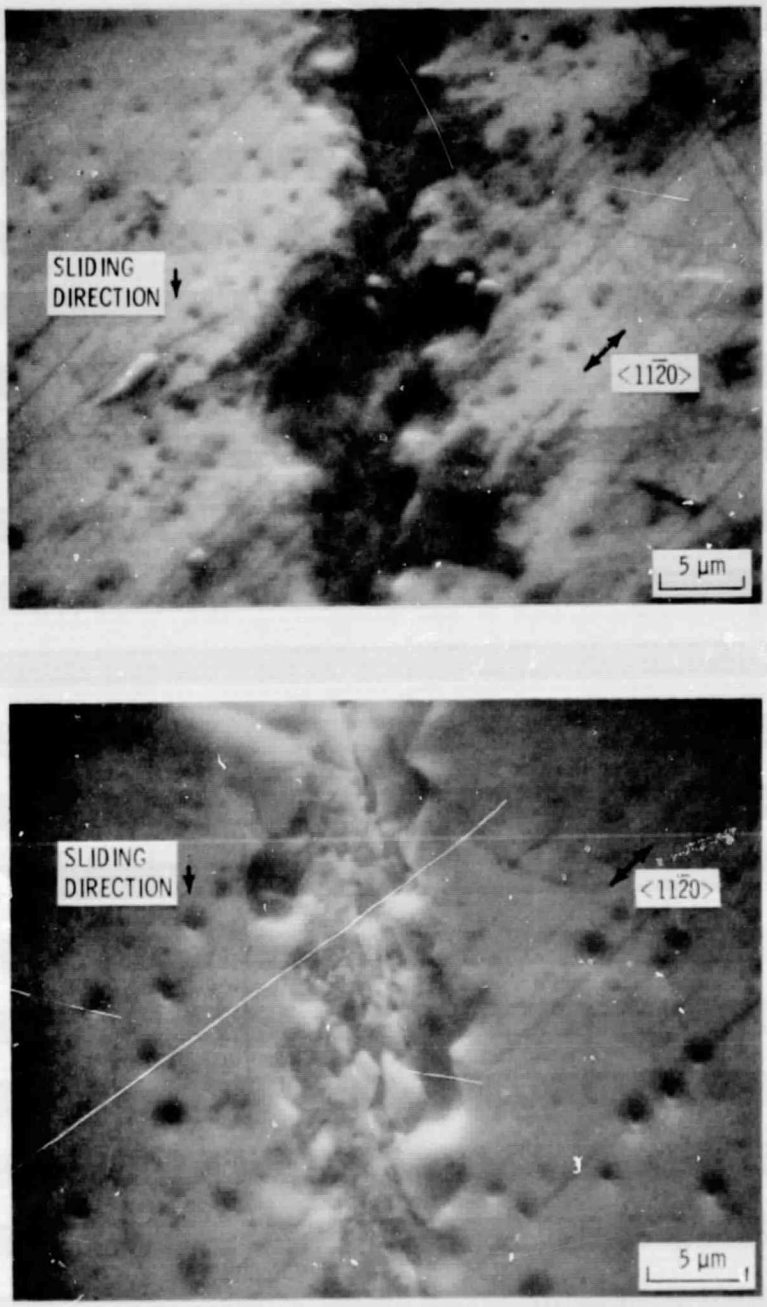

Figure 16. - Scanning electron micrographs of wear tracks on a (0001) silicon carbide surface. Etched with molten salt. Single pass of conical diamond rider; sliding direction, <10$\bar{1}$0>; sliding velocity, 3 mm/min; load, 50 grams; temperature, 25^0 C in argon at atmospheric pressure.

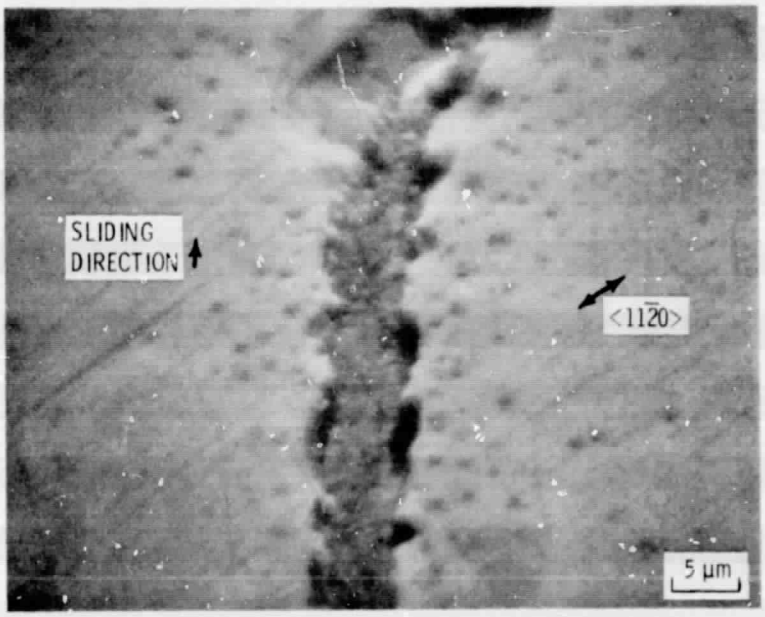

Figure 16. - Concluded.